Henning Bonart, Christian Kahle, Jens-Uwe Repke

Comparison of energy stable simulation of moving contact line problems using a thermodynamically consistent Cahn–Hilliard Navier–Stokes model

Bonart, H., Kahle, C., & Repke, J.-U. (2019). Comparison of energy stable simulation of moving contact line problems using a thermodynamically consistent Cahn–Hilliard Navier–Stokes model. Journal of Computational Physics, 399, 108959. https://doi.org/10.1016/j.jcp.2019.108959

Comparison of Energy Stable Simulation of Moving Contact Line Problems using a Thermodynamically Consistent Cahn–Hilliard Navier–Stokes Model*

Henning Bonart[a,*], Christian Kahle[b], Jens-Uwe Repke[a]

[a] *Process Dynamics and Operations Group, Technische Universität Berlin, 10623 Berlin, Germany*
[b] *Center for Mathematical Sciences, Technische Universität München, 85748 Garching bei München, Germany*

Abstract

Liquid droplets sliding along solid surfaces are a frequently observed phenomenon in nature, e.g., raindrops on a leaf, and in everyday situations, e.g., drops of water in a drinking glass. To model this situation, we use a phase field approach. The bulk model is given by the thermodynamically consistent Cahn–Hilliard Navier–Stokes model from [Abels et al., Math. Mod. Meth. Appl. Sc., 22(3), 2012]. To model the contact line dynamics we apply the generalized Navier boundary condition for the fluid and the dynamically advected boundary contact angle condition for the phase field as derived in [Qian et al., J. Fluid Mech., 564, 2006]. In recent years several schemes were proposed to solve this model numerically. While they widely differ in terms of complexity, they all fulfill certain basic properties when it comes to thermodynamic consistency. However, an accurate comparison of the influence of the schemes on the moving contact line is rarely found. Therefore, we thoughtfully compare the quality of the numerical results obtained with three different schemes and two different bulk energy potentials. Especially, we discuss the influence of the different schemes on the apparent contact angles of a sliding droplet.

Keywords: Multiphase flows, Drop phenomena, Contact line dynamics, Phase field modeling
2000 MSC: 35Q30, 35Q35, 76D05, 76M10, 76T99

*The first and third author acknowledge the North-German Supercomputing Alliance (HLRN) for providing HPC resources that have contributed to the research results reported in this paper and thank the German Research Foundation (DFG) for the financial support within the project RE 1705/16-1. The second author gratefully acknowledges the support by the German Research Foundation (DFG) through the International Research Training Group IGDK 1754 "Optimization and Numerical Analysis for Partial Differential Equations with Nonsmooth Structures".

*Corresponding author
Email addresses: henning.bonart@tu-berlin.de (Henning Bonart), christian.kahle@ma.tum.de (Christian Kahle), jens-uwe.repke@tu-berlin.de (Jens-Uwe Repke)

1. Introduction

Liquid droplets sliding along solid surfaces are a frequently observed phenomenon in nature, e.g., raindrops on a leaf, and in everyday situations, e.g., drops of water in a drinking glass. Furthermore, sliding droplets (and consequently the suppression of those) are crucial in many industrial applications such as coating or painting and separation or reaction processes involving multiple phases and thin liquid films. The position where the interface between the sliding droplet and the surrounding fluid intersects the solid surface is the moving contact line (or contact point if a two dimensional problem is observed). For details about liquids on surfaces and moving contact lines see the reviews [1, 2] and the references therein. In a continuum approach, applying the common no-slip boundary condition at the solid surface close to the contact line leads to a non-physical, logarithmically diverging energy dissipation. One possibility to circumvent this difficulty is the coupling of the incompressible Navier–Stokes equations with the Cahn–Hilliard equation [3]. This phase field method models the interface between the fluids with a diffuse interface of positive thickness and describes the distribution of the different fluids by a smooth indicator function. Especially, the Cahn–Hilliard equation allows the contact line to move naturally on the solid surface due to a diffusive flux across the interface, which is driven by the gradient of the chemical potential. Furthermore, the phase field method is able to calculate topological changes like breakup of droplets or merging interfaces [4]. For example in experiments by [5, 6], it is found that during the rapid spreading of a droplet the contact angle can differ from the equilibrium angle given by Young's equation. To allow for nonequilibrium contact angles, [3] proposes a relaxation of the static contact angle boundary condition, see Section 1.1, and [7] extends this approach to include the slip at the contact line stemming from the uncompensated Young stress.

In [8] a thermodynamically consistent Cahn–Hilliard Navier–Stokes phase field model is proposed to describe the dynamics of the two phases in the bulk domain. It is valid also for different densities of the involved fluids, but specific contact line dynamics are not included. Recently, several numerical schemes for solving this system have been proposed, see for example, [9–13]. All these schemes are thermodynamically consistent in the sense, that they mimic the energy law from [8] in the time discrete or even in the fully discrete setting. They range from fully coupled and nonlinear to decoupled and linear, where decoupled means, that the Navier–Stokes and the Cahn–Hilliard equations are solved sequentially.

These schemes are extended to the Cahn–Hilliard Navier–Stokes system with moving contact lines in various papers. Here the concepts from the aforementioned papers for the discretization of the bulk equations are straightforwardly applied. For the case of equal densities, schemes are proposed, e.g., in [14–17] and for the case of different densities in [11, 18]. The model from [8] contains an

additional flux term in the momentum equation, that renders the model thermodynamically consistent. This term is often neglected, see e.g., [19]. For the resulting model several discretization schemes are proposed and we refer to the references in [18] for details. In all these simulations involving moving contact lines a polynomial bulk energy potential is applied. In contrast, we include a double obstacle potential, which is subsequently relaxed, see [20]. In [9, 21] in a numerical benchmark setting the results with this kind of energy are typically closer to sharp interface numeric than with the polynomial potential.

To prepare future research on the passive control of droplets sliding on structured or chemically patterned surfaces, we extend the work of [9] in this paper to the case of moving contact line dynamics and compare the numerical results with the corresponding decoupled scheme from, e.g., [11] and a fully linear scheme, that both uses decoupling and stabilization as in [16]. We test both the polynomially and the relaxed double-obstacle bulk energy potential, so that in total we compare six different combinations of bulk energy potentials and solution schemes.

The remainder of the paper is organized as follows. In the second part of the introduction, Section 1.1, we introduce the continuous model as well as the bulk energy potentials and the contact line energies. Afterwards, we derive a weak formulation in Section 2 and the numerical schemes in Section 3. In Section 4.1 we compare the different combinations at first in the bulk without any contact line. Finally, we compare simulation results of sliding droplets on inclined surfaces to investigate the accuracy and efficiency of the linearization and decoupling strategies as well as the bulk energy potentials for moving contact line problems in Section 4.2. We conclude our work in Section 5.

1.1. Model

In the fluid domain we consider the thermodynamically consistent model for the simulation of two-phase flow presented in [8], in the variant for nonlinear density functions proposed in [22, Eq. 1.10]. To model the contact line dynamics we use generalized Navier boundary conditions for the velocity field together with dynamically advected boundary conditions for the phase field as proposed in [7].

In strong form the model reads as follows. Let $\Omega \subset \mathbb{R}^d$ with $d \in \{2, 3\}$ denote an open, polygonally/polyhedrally bounded Lipschitz domain and $I = (0, T]$ with $0 < T < \infty$ denote a time interval. The outer unit normal on $\partial\Omega$ is ν_Ω. At time $t \in I$ the primal variables are given by the velocity field v, the pressure field p, the phase field φ and the chemical potential μ. They satisfy the following

system of equations

$$\rho\partial_t v + ((\rho v + J)\cdot\nabla)v + R\frac{v}{2} - \operatorname{div}(2\eta Dv) + \nabla p = -\varphi\nabla\mu + \rho g \quad \text{in } \Omega, \quad (1)$$

$$-\operatorname{div}(v) = 0 \quad \text{in } \Omega, \quad (2)$$

$$\partial_t\varphi + v\cdot\nabla\varphi - b\Delta\mu = 0 \quad \text{in } \Omega, \quad (3)$$

$$-\sigma\epsilon\Delta\varphi + \frac{\sigma}{\epsilon}W'(\varphi) = \mu \quad \text{in } \Omega, \quad (4)$$

$$v\cdot\nu_\Omega = 0 \quad \text{on } \partial\Omega, \quad (5)$$

$$[2\eta Dv\nu_\Omega + l(\varphi)v_{tan} - L(\varphi)\nabla\varphi]\times\nu_\Omega = 0 \quad \text{on } \partial\Omega, \quad (6)$$

$$rB + L(\varphi) = 0 \quad \text{on } \partial\Omega, \quad (7)$$

$$\nabla\mu\cdot\nu_\Omega = 0 \quad \text{on } \partial\Omega, \quad (8)$$

where we abbreviate $J := -b\frac{\partial\rho}{\partial\varphi}\nabla\mu$, $R := -b\nabla\frac{\partial\rho}{\partial\varphi}\cdot\nabla\mu$, $B := \partial_t\varphi + v\cdot\nabla\varphi$, $L := \sigma\epsilon\nabla\varphi\cdot\nu_\Omega + \gamma'(\varphi)$. The gravitational acceleration is denoted by g and we abbreviate $2Dv := \nabla v + (\nabla v)^t$. The function $W(\varphi)$ denotes a dimensionless potential of double-well type, with two strict minima at ±1. We refer to Remark 2 for a discussion of possible choices for W. We formulate (1) with a shifted pressure variable $p = p^{phys} - \mu\varphi$, where p^{phys} denotes the physical pressure.

The contact line energy is denoted by γ, see Remark 3. The strictly positive, constant parameters for the equations in Ω are given by the mobility $b > 0$, the scaled surface tension σ, see Remark 2, and the interfacial thickness parameter ϵ. The constant mobility is used for simplicity but the following is also valid for mobilities that depend on φ.

The (nonlinear) density function is denoted by $\rho \equiv \rho(\varphi) > 0$ and satisfies $\rho(-1) = \rho_1$ and $\rho(1) = \rho_2$, with $\rho_2 > \rho_1 > 0$ denoting the constant densities of the two involved fluids. The (nonlinear) viscosity function is $\eta \equiv \eta(\varphi) > 0$ and satisfies $\eta(-1) = \eta_1$ and $\eta(1) = \eta_2$, with η_1, η_2 denoting the viscosities of the involved fluids.

Remark 1 (Nonlinear density and viscosity)**.** *In general there is no quantitative upper bound available for φ and thus in particular $|\varphi| > 1$ is possible. Thus a linear relation between φ and ρ can lead to negative densities in practice. This might appear for especially large density ratios, compare for example [11, Rem. 4.1]. Note, that φ can be proven to be bounded in L^∞ if W'' is uniformly bounded, see e.g. [23].*

It is a common approach to cut φ when inserting it into the linear function for ρ, see e.g. [18]. This leads to a nonsmooth relation between φ and ρ. However, as we require differentiability of ρ to define R and J this is not admissible here. A second approach is to clip ρ of at some positive value, see e.g. [11, 24]. This leads to a uniform bound on ρ based on the Atwood number $At = \frac{\rho_2-\rho_1}{\rho_2+\rho_1}$. Here we use the latter approach and define ρ as the following smooth, monotone

and strictly positive function

$$\rho(\varphi) = \begin{cases} \frac{1}{4}\rho_1 & \text{if } \varphi \leq -At^{-1}, \\ \frac{1}{\rho_1}\left(\frac{\rho_2-\rho_1}{2}\varphi + \frac{\rho_2+\rho_1}{2}\right)^2 + \frac{1}{4}\rho_1 & \text{if } -At^{-1} < \varphi < -1 - \frac{\rho_1}{\rho_2-\rho_1}, \\ \frac{\rho_2-\rho_1}{2}\varphi + \frac{\rho_2+\rho_1}{2} & \text{if } -1 - \frac{\rho_1}{\rho_2-\rho_1} \leq \varphi \leq 1 + \frac{\rho_1}{\rho_2-\rho_1}, \\ -\frac{1}{\rho_1}\left(\frac{\rho_2-\rho_1}{2}\varphi - \frac{\rho_2+\rho_1}{2}\right)^2 + \rho_2 + \frac{3}{4}\rho_1 & \text{if } 1 + \frac{\rho_1}{\rho_2-\rho_1} < \varphi < At^{-1}, \\ \rho_2 + \frac{3}{4}\rho_1 & \text{if } At^{-1} \leq \varphi. \end{cases} \tag{9}$$

For a discussion we refer to [24, Rem. 2.1]. The nonlinear viscosity $\eta(\varphi)$ can be defined analogously.

We note, that the total mass $\int_\Omega \rho(\varphi)\,dx$ is only conserved if $\rho(\varphi)$ is a linear function on the (a-priori unknown) image of φ, see e.g., [9, Rem. 1], while $\int_\Omega \varphi\,dx$ is a conserved quantity,

As boundary data we use generalized Navier boundary conditions for the velocity field and dynamically advected contact angle boundary conditions for the two-phase equation, see [7, Eq. 4.4, Eq. 4.5]. Here γ denotes the fluid-solid interfacial free energy, see [7, Sec. 4], $l(\varphi)$ is a slip coefficient for the generalized Navier boundary condition applied to the tangential part of the velocity $v_{tan} := v - (v \cdot \nu_\Omega)\nu_\Omega$, while $L(\varphi)\nabla\varphi \times \nu_\Omega$ is the uncompensated Young stress and L is the chemical potential at the solid surface. The static contact angle is denoted by θ_s and $r \geq 0$ is a phenological parameter allowing for nonequilibrium at the contact line. For $r \equiv 0$ (7) reduces to $\sigma\epsilon\nabla\varphi \cdot \nu_\Omega = -\gamma'(\varphi)$, which means, that a static contact angle at the interface is assumed. Furthermore, for $\gamma'(\varphi) \equiv 0$ (or rather $\theta_s \equiv 90°$, see Remark 3), (7) further simplifies to $\nabla\varphi \cdot \nu_\Omega = 0$, which is a no-flux condition for φ at the solid surface. The no-slip condition for v is obtained from (6) by $L \equiv 0$ and $l \to \infty$ (or rather the slip length $l_s \equiv 0$, see Remark 12).

Concerning the existence of solutions to (1) to (5) and (8) together with no-slip for v and a homogeneous Neumann (or no-flux) boundary condition for φ as well as with different assumptions on b and W, we refer to [22, 24–26]. For the boundary conditions considered here we are not aware of such results, but refer to [27] for the Cahn–Hilliard Navier–Stokes system with equal densities, to [28] for analytical results for the Cahn–Hilliard system with dynamic boundary conditions, and to [11] for a Cahn–Hilliard Navier–Stokes model with dynamical contact angle condition, but no-slip condition for the Navier–Stokes equation. Concerning sharp interface limits, we refer to [8] for the bulk model with homogeneous boundary conditions. Sharp interface analysis for the model with equal densities including contact line dynamics is available in [29].

For (1) to (5) and (8) together with no-slip for v and no-flux for φ, several thermodynamically consistent discretization schemes were proposed in the last years. Here, we refer to [9, 10, 13]. Especially in [9] the influence of spatial adaptivity on the fully discrete energy law is discussed. We further refer to [12], where the benefit of using fully coupled schemes is shown numerically, and to

[30] for an extensive discussion of several discretization schemes for the bulk energy potential W^{poly}. For the full model (1)–(8) thermodynamically consistent schemes are for example proposed in [17] for the case of constant density, and in [18] for the general case. The case with no-slip boundary condition for v and dynamically advected boundary condition for φ is numerically and analytically considered in [11].

Remark 2 (Bulk energy potentials)**.** *Throughout this work we consider polynomially bounded potentials for W. To state the precise assumptions we split $W = W_+ + W_-$ with W_+ denoting the convex part of W and W_- denoting the concave part. We assume that $W : \mathbb{R} \to \mathbb{R}$ is continuously differentiable and that W and its derivatives W'_+ and W'_- are polynomially bounded, i.e., there exists $C > 0$ such that*

$$|W(\varphi)| \leq C(1 + |\varphi|^4), \quad |W'_+(\varphi)| \leq C(1 + |\varphi|^3), \quad |W'_-(\varphi)| \leq C(1 + |\varphi|^3).$$

Note, that these bounds on the polynomial degree might be relaxed, see [9, (A3)], and that these assumptions are used to show the existence of discrete solutions.

These assumptions are for example fulfilled by the commonly used polynomial potential

$$W^{poly}(\varphi) := \frac{1}{4}(1-\varphi^2)^2, \quad W^{poly_2}(\varphi) := \begin{cases} \frac{1}{4}(1-\varphi^2)^2 & \text{if } |\varphi| \leq 1, \\ (|\varphi|-1)^2 & \text{else,} \end{cases}$$

where W^{poly_2} is a modification of W^{poly} that guarantees an L^∞ bound on φ, see [23].

Another potential that fulfills the assumptions is

$$W^s(\varphi) := \frac{1}{2}\left(1 - (\xi\varphi)^2 + s\lambda(\xi\varphi)^2\right) + \theta,$$

where $\lambda(x) := \max(0, x-1) + \min(0, x+1)$, $\theta := \frac{1}{2(s-1)}$ and $\xi := \frac{s}{s-1}$ are chosen such that $W(\pm 1) \equiv 0$ are the two minima of W^s. Here $s \gg 1$ is a penalization parameter. It appears as Moreau–Yosida relaxation of the double obstacle potential W^∞, see [20, 31]. In a synthetic rising bubble benchmark, [32], our results with this potential are typically closer to the results from sharp interface methods than with the potential W^{poly}, see [9, Tab. 1].

In the following, whenever we use the letter W, we mean any of the three mentioned bulk energy potentials.

In preparation of later results, we state the splittings of the potentials W into $W(\varphi) = W_+(\varphi) + W_-(\varphi)$. These are

$$W_+^{poly}(\varphi) = \frac{1}{4}\varphi^4 - \frac{1}{4}, \qquad W_-^{poly}(\varphi) = \frac{1}{2}(1-\varphi^2),$$

$$W_+^{poly_2}(\varphi) = \begin{cases} \frac{1}{4}\varphi^4 - \frac{1}{4} & \text{if } |\varphi| \leq 1, \\ (|\varphi|-1)^2 - \frac{1}{2}(1-\varphi^2) & \text{if } |\varphi| > 1, \end{cases} \qquad W_-^{poly_2}(\varphi) = \frac{1}{2}(1-\varphi^2),$$

$$W_+^s(\varphi) = \frac{s}{2}\lambda(\xi\varphi)^2 + \theta, \qquad W_-^s(\varphi) = \frac{1}{2}(1-(\xi\varphi)^2).$$

These splittings are not unique, and we refer for example to [33] for an alternative splitting of W^{poly_2}. We further refer to [30] for a discussion on the dissipation that is introduced by the convex-concave splitting and also for an elaborated discussion on the dissipation that in general is introduced by splitting W. In our numerical tests, splittings that have a quadratic convex part and thus give linear systems, typically lead to broader interfaces during the simulation and require smaller time steps to prevent this effect. Thus it is favorable to use non-linear systems as obtained by the proposed splittings above.

To define the scaled surface tension σ we introduce the constant c_W as $c_W^{-1} = \int_{-\infty}^{\infty} 2W(\Phi_0(z))\,dz = \int_{-\infty}^{\infty} (\partial_z \Phi_0(z))^2\,dz$, where Φ_0 denotes the first order approximation of φ depending on W. It satisfies $\Phi_0(z)_{zz} = W'(\Phi_0(z))$, see [8, Sec. 4.3.3]. Then $\sigma = c_W \sigma_{12}$, where σ_{12} denotes the physical value of the surface tension between phase 1 and phase 2. As the dynamics of the diffuse model depend on the particular form of W, this scaling is necessary to guarantee that the same sharp interface dynamic is approximated independently of W. Using W^{poly} and W^{poly_2} it holds $\Phi_0(z) = \tanh(z/\sqrt{2})$ and $c_W = \frac{3}{2\sqrt{2}}$. For W^s one obtains by elementary calculation

$$\Phi_0(z) = \begin{cases} -\Phi_0(-z) & \text{if } z < 0, \\ \sqrt{\xi}^{-1} \sin(\xi z) & \text{if } 0 \le z \le z_0 := \xi^{-1} \arctan(\sqrt{s-1}), \\ 1 - s^{-1} \exp(-\xi\sqrt{s-1}(z - z_0)) & \text{if } z > z_0, \end{cases}$$

and

$$c_W^{-1} = (1 - s^{-2}) \arctan(\sqrt{s-1}) + s^{-2}(s+2)\sqrt{s-1}.$$

For $s \to \infty$ we recover the well-known scaling $c_W = \frac{2}{\pi}$ for the double-obstacle potential.

Remark 3 (Contact line energy)**.** *The basic formula to derive the contact line energy is given by Young's law, namely*

$$\sigma_{s1} - \sigma_{s2} = \sigma_{12} \cos\theta_s.$$

Here σ_{s1} and σ_{s2} denote the physical surface tensions between phase 1 ($\varphi = -1$) and the solid (σ_{s1}) and phase 2 ($\varphi = 1$) and the solid (σ_{s2}). Further σ_{12} denotes the surface tension between phase 1 and phase 2 and θ_s denotes the static equilibrium contact angle between the solid and the interface and is measured in phase 2.

We use the ansatz

$$\gamma(\varphi) := \frac{\sigma_{s1} + \sigma_{s2}}{2} - \sigma_{12} \cos\theta_s \vartheta(\varphi)$$

and choose $\vartheta(\varphi)$ to fulfill

$$\gamma(-1) = \sigma_{s1}, \quad \gamma(0) = \frac{\sigma_{s1} + \sigma_{s2}}{2}, \quad \gamma(1) = \sigma_{s2}, \quad \gamma'(\pm 1) = 0.$$

In particular it holds, that $\vartheta(-1) = -\frac{1}{2}$ *and* $\vartheta(1) = \frac{1}{2}$*. Here, the unscaled value of the surface tension appears as can be shown by matched asymptotic expansions, see [8, Sec. 4.3.4].*

Common choices for ϑ *contain the sine function* $\vartheta^{\sin}(\varphi) := \frac{1}{2}\sin(\frac{\pi}{2}\varphi)$*, for example proposed in [7, Sec. 4], or a cubic polynomial* $\vartheta^{poly}(\varphi) = \frac{1}{4}(3\varphi - \varphi^3)$*, for example proposed in [29]. An alternative is given in [34]. Here the assumption of equipartition of energy, i.e.,* $\frac{\epsilon}{2}|\nabla\varphi|^2 \approx \frac{1}{\epsilon}W(\varphi)$*, is used to derive* $(\vartheta^W)'(\varphi) = c_W\sqrt{2W(\varphi)}$*. Finally, we state a contact line energy, that is the sum of a convex and a concave function namely* $\vartheta^{cc}(\varphi) = \vartheta^{cc}_+(\varphi) + \vartheta^{cc}_-(\varphi)$ *with*

$$\vartheta^{cc}_+(\varphi) = \begin{cases} -\frac{1}{2} & \text{if } \varphi \le -1, \\ \frac{1}{2}(\varphi+1)^2 - \frac{1}{2} & \text{if } \varphi \in (-1,0), \\ \varphi & \text{if } \varphi \ge 0, \end{cases} \quad \vartheta^{cc}_-(\varphi) = \begin{cases} 0 & \text{if } \varphi \le 0, \\ -\frac{1}{2}\varphi^2 & \text{if } \varphi \in (0,1), \\ \frac{1}{2} - \varphi & \text{if } \varphi \ge 1. \end{cases}$$

Here ϑ^{cc}_+ *is convex and* ϑ^{cc}_- *is concave and* $\vartheta^{cc} \in C^{1,1}(\mathbb{R})$ *with* $\vartheta'' \in L^\infty(\mathbb{R})$*.*

Note, that for any ϑ *that has a bounded second derivative, we can define a convex-concave splitting via*

$$\vartheta_+(\varphi) = \vartheta(\varphi) + \frac{1}{2}\max_{\phi\in\mathbb{R}}(\vartheta''(\phi))\varphi^2, \qquad \vartheta_-(\varphi) = -\frac{1}{2}\max_{\phi\in\mathbb{R}}(\vartheta''(\phi))\varphi^2,$$

compare [35]. This is very similar to the stabilization approach, proposed for example in [16], that essentially resembles one of Eyre's linear schemes [30]. In the following we always assume a convex-concave splitting of γ*. This approach can also be used for the potential* W*.*

Remark 4. *To the best of our knowledge, there is no consent yet which combinations of bulk energy potential and contact line energy are most appropriate from both a physical and numerical point of view. From an analytical point of view, all combinations are reasonable that lead to the correct sharp interface limit, see [29] for results on formal sharp interface asymptotics. Here, the authors use the combination of* W^{poly} *and* ϑ^{poly}*. However, this topic is subject to future work. Further note, that using the notation from [29] we are in the setting* $L_d = \mathcal{O}(\epsilon)$*, and* $V_s = \mathcal{O}(1)$*.*

2. The weak formulation

We next derive the weak formulation that is the basis for our numerical scheme proposed in Section 3. We assume sufficient regularity of all appearing functions. Multiplying (3) with $\frac{\partial\rho}{\partial\varphi}$ we observe

$$\partial_t\rho + \operatorname{div}(\rho v + J) = R. \tag{10}$$

Note that if ρ is a nonlinear function $R \neq 0$ holds and thus mass conservation can be violated as soon as a nonlinear function for ρ is used to guarantee $\rho > 0$.

Note that the conservation of φ is not affected. Using (10) the momentum equation (1) can equivalently be written as

$$\partial_t(\rho v) + \operatorname{div}(v \otimes (\rho v + J)) - R\frac{v}{2} - \operatorname{div}(2\eta Dv) + \nabla p = -\varphi\nabla\mu + \rho g, \qquad (11)$$

see [22, Eq. (1.12)]. We stress that this reformulation is independent of the actual boundary condition.

To define the weak formulation we multiply both (1) and (11) by a solenoidal test function $\frac{1}{2}w$ that satisfies $w|_{\partial\Omega}\cdot\nu_\Omega = 0$ and sum up the equations to achieve

$$\begin{aligned}\frac{1}{2}\int_\Omega (\rho\partial_t v + \partial_t(\rho v))\cdot w\,dx - \int_\Omega \operatorname{div}(2\eta Dv)\cdot w\,dx + \int_\Omega (\varphi\nabla\mu - \rho g)\cdot w\,dx \\ + \frac{1}{2}\int_\Omega ((\rho v + J)\cdot\nabla)v\cdot w\,dx + \frac{1}{2}\int_\Omega \operatorname{div}(v\otimes(\rho v+J))\cdot w\,dx = 0.\end{aligned}$$

Using integration by parts together with the boundary conditions $v\cdot\nu_\Omega = 0$ and $\nabla\mu\cdot\nu_\Omega = 0$ we observe

$$\begin{aligned}&\frac{1}{2}\int_\Omega ((\rho v + J)\cdot\nabla)v\cdot w\,dx + \frac{1}{2}\int_\Omega \operatorname{div}(v\otimes(\rho v+J))\cdot w\,dx\\ =&\frac{1}{2}\int_\Omega ((\rho v + J)\cdot\nabla)v\cdot w - ((\rho v+J)\nabla)w\cdot v\,dx\\ =:&a(\rho v + J, v, w).\end{aligned}$$

Note that $a(\cdot, v, v) = 0$ holds. Using integration by parts for the viscous stress we observe

$$\begin{aligned}-\int_\Omega \operatorname{div}(2\eta Dv)\cdot w\,dx &= \int_\Omega 2\eta Dv : Dw\,dx - \int_{\partial\Omega} 2\eta Dv\nu_\Omega\cdot w\,ds,\\ &= \int_\Omega 2\eta Dv : Dw\,dx + \int_{\partial\Omega}(l(\varphi)v_{tan} + rB\nabla\varphi)\cdot w\,ds\end{aligned}$$

where $Dv : Dw := \sum_{ij=1}^n (Dv)_{ij}(Dw)_{ij}$ and we use the boundary conditions (6) and (7).

The weak form of (3)–(4) is derived by the standard procedure. Summarizing the equations, we obtain the following weak form of (1)–(8):

Definition 5 (The weak formulation)**.** *Find sufficiently smooth v, μ, φ, with v solenoidal, $v\cdot\nu_\Omega = 0$, such that for all w, ψ, ϕ, with w solenoidal, the following*

equations are satisfied:

$$\frac{1}{2}\int_\Omega (\rho\partial_t v + \partial_t(\rho v))\cdot w\,dx + a(\rho v + J, v, w) + \int_\Omega 2\eta Dv : Dw\,dx$$
$$+\int_{\partial\Omega}(l(\varphi)v_{tan} + rB(\varphi_t,\varphi,v)\nabla\varphi)\cdot w\,ds - \int_\Omega(-\varphi\nabla\mu + \rho g)\cdot w\,dx = 0, \quad (12)$$
$$\int_\Omega \varphi_t\psi\,dx - \int_\Omega \varphi v\cdot\nabla\psi\,dx + \int_\Omega b\nabla\mu\cdot\nabla\psi\,dx = 0, \quad (13)$$
$$\int_\Omega \sigma\epsilon\nabla\varphi\cdot\nabla\phi + \frac{\sigma}{\epsilon}W'(\varphi)\phi\,dx - \int_\Omega \mu\phi\,dx$$
$$+\int_{\partial\Omega}(rB(\varphi_t,\varphi,v) + \gamma'(\varphi))\,\phi\,ds = 0. \quad (14)$$

The weak form (12)–(14) allows us to derive the following energy identity.

Theorem 6 (The formal energy identity)**.** *Assume there exists a sufficiently smooth solution to* (12)–(14)*. Then the following energy identity holds*

$$\frac{d}{dt}\left(\int_\Omega \frac{1}{2}\rho|v|^2\,dx + \sigma\int_\Omega \frac{\epsilon}{2}|\nabla\varphi|^2 + \frac{1}{\epsilon}W(\varphi)\,dx + \int_{\partial\Omega}\gamma\,ds\right)$$
$$+\int_\Omega 2\eta|Dv|^2\,dx + \int_\Omega b|\nabla\mu|^2\,dx \quad (15)$$
$$+\int_{\partial\Omega} l(\varphi)|v_{tan}|^2\,ds + r\int_{\partial\Omega}|B(\varphi_t,\varphi,v)|^2\,ds = \int_\Omega \rho g\cdot v\,dx.$$

Note that the energy in the system can only increase by the gravitational acceleration.

Proof. Use $w \equiv v$, $\Psi \equiv \mu$, and $\Phi \equiv \partial_t\varphi$ as test functions in (12)–(14) and sum up the resulting equations. □

3. The numerical schemes

For a practical implementation in a finite element scheme we introduce a time grid $0 = t_0 < t_1 < \ldots < t_{m-1} < t_m < \ldots < t_M = T$ on $I = [0, T]$. For the sake of notational simplicity let the time grid be equidistant with step size $\tau > 0$. We further introduce a triangulation $\mathcal{T}_h$ of $\overline{\Omega}$ into cells T_i, such that $\mathcal{T}_h = \bigcup_{i=1}^N T_i$ covers $\overline{\Omega}$ exactly.

On $\mathcal{T}_h$ we introduce the finite element spaces

$$V_1 := \{v \in C(\overline{\Omega}) \,|\, v|_{T_i} \in \mathcal{P}_1\},$$
$$V_2 := \{v \in C(\overline{\Omega})^d \,|\, v|_{T_i} \in (\mathcal{P}_2)^2,\ v\cdot\nu_\Omega = 0\},$$

where $\mathcal{P}_k$ denotes the space of polynomials of order up to k. We use V_1 to define discrete approximations φ_h, μ_h, and p_h of the corresponding continuous variables, and V_2 to define the discrete approximation v_h of v. This means that

we use standard Taylor–Hood elements for the Navier–Stokes part and explicitly denote the pressure variable in the following.

The scheme reads as follows:
Given $\varphi^{m-1} \in V_1$, $\mu^{m-1} \in V_1$, and $v^{m-1} \in V_2$, find $\varphi_h^m \in V_1$, $\mu_h^m \in V_1$, $p_h^m \in V_1$ and $v_h^m \in V_2$, such that for all $w \in V_2$, $q \in V_1$, $\Phi \in V_1$, and $\Psi \in V_1$ the following equations hold

$$\begin{aligned}
&\frac{1}{\tau}\left(\frac{\rho^m + \rho^{m-1}}{2} v_h^m - \rho^{m-1} v^{m-1}, w\right) \\
&+a(\rho^{m-1} v^{m-1} + J^{m-1}, v_h^m, w) + (2\eta^{m-1} D v_h^m, Dw) - (\mathrm{div} w, p_h^m) \\
&+(l(\varphi^{m-1}) v_{h,tan}^m + r B_h^m \nabla \varphi^{m-1}, w)_{\partial\Omega} \\
&+(\varphi^{m-1} \nabla \mu_h^m, w) - (g\rho^{m-1}, w) = 0, \quad (16)\\
&-(\mathrm{div} v_h^m, q) = 0, \quad (17)\\
&\frac{1}{\tau}(\varphi_h^m - \varphi^{m-1}, \Psi) - (\varphi^{m-1} v_h^m, \nabla\Psi) + (b\nabla\mu_h^m, \nabla\Psi) = 0, \quad (18)\\
&\sigma\epsilon(\nabla\varphi_h^m, \nabla\Phi) + \frac{\sigma}{\epsilon}(W_+'(\varphi_h^m) + W_-'(\varphi^{m-1}), \Phi) - (\mu_h^m, \Phi) \\
&+ (r B_h^m, \Phi)_{\partial\Omega} + \left(\gamma_+'(\varphi_h^m) + \gamma_-'(\varphi^{m-1}), \Phi\right)_{\partial\Omega} = 0, \quad (19)
\end{aligned}$$

with $J^{m-1} := -b\frac{\partial\rho}{\partial\varphi}(\varphi^{m-1})\nabla\mu^{m-1}$, $B_h^m := \left(\frac{\varphi_h^m - \varphi^{m-1}}{\tau} + v_h^m \cdot \nabla\varphi^{m-1}\right)$, $\rho^{m-1} := \rho(\varphi^{m-1})$, and $\eta^{m-1} := \eta(\varphi^{m-1})$.

Using Brouwer's fixed-point theorem one can show the existence of at least one solution following [9, Thm. 2]. The uniqueness stays unclear due to the nonlinearity $\rho^m v_h^m$ in (16). The scheme fulfills a fully discrete variant of the formal energy identity (15).

Theorem 7 (The fully discrete energy inequality)**.** *Let $\varphi_h^m \in V_1^m$, $\mu_h^m \in V_1^m$, and $v_h^m \in V_2^m$ denote a solution to* (16)–(19)*. Then the following energy inequality holds*

$$\begin{aligned}
&\frac{1}{\tau}\left(\frac{1}{2}\int_\Omega \rho^m |v_h^m|^2 + \sigma\int_\Omega \frac{\epsilon}{2}|\nabla\varphi_h^m|^2 + \frac{1}{\epsilon}W(\varphi_h^m)\,dx + \int_{\partial\Omega}\gamma(\varphi_h^m)\,ds\right) \\
&+\int_\Omega 2\eta^{m-1}|Dv_h^m|^2\,dx + b\int_\Omega |\nabla\mu_h^m|^2\,dx + \int_{\partial\Omega} l(\varphi^{m-1})|v_{h,tan}^m|^2\,ds + r\int_{\partial\Omega}|B_h^m|^2\,ds \\
&+\frac{1}{\tau}\left(\frac{1}{2}\int_\Omega \rho^{m-1}|v_h^m - v^{m-1}|^2\,dx + \frac{\sigma\epsilon}{2}\int_\Omega |\nabla\varphi_h^m - \nabla\varphi^{m-1}|^2\,dx\right) \\
&\le \frac{1}{\tau}\left(\frac{1}{2}\int_\Omega \rho^{m-1}|v^{m-1}|^2 + \sigma\int_\Omega\frac{\epsilon}{2}|\nabla\varphi^{m-1}|^2 + \frac{1}{\epsilon}W(\varphi^{m-1})\,dx + \int_{\partial\Omega}\gamma(\varphi^{m-1})\,ds\right) \\
&+\int_\Omega \rho^{m-1} g\cdot v_h^m\,dx.
\end{aligned}$$

Proof. We use $w \equiv v_h^m$, $q = p_h^m$, $\Psi \equiv \mu_h^m$ and $\Phi \equiv \frac{\varphi_h^m - \varphi^{m-1}}{\tau}$ as test functions

in (16)–(19) and sum up to obtain

$$\begin{aligned}
\frac{1}{\tau}\left(\frac{1}{2}\int_\Omega \rho^m|v_h^m|^2-\frac{1}{2}\int_\Omega \rho^{m-1}|v^{m-1}|^2+\frac{1}{2}\int_\Omega \rho^{m-1}|v_h^m-v^{m-1}|^2\,dx\right)\\
+\int_\Omega 2\eta^{m-1}|Dv_h^m|^2\,dx-\int_\Omega \rho^{m-1}g\cdot v_h^m\,dx\\
+\int_{\partial\Omega} l(\varphi^{m-1})v_{h,tan}^m\cdot v_h^m\,ds+r\int_{\partial\Omega} B_h^m\nabla\varphi^{m-1}\cdot v_h^m\,ds\\
+b\int_\Omega |\nabla\mu_h^m|^2\,dx\\
+\frac{\sigma\epsilon}{2\tau}\left(\int_\Omega |\nabla\varphi_h^m|^2-|\nabla\varphi^{m-1}|^2+|\nabla\varphi_h^m-\nabla\varphi^{m-1}|^2\,dx\right)\\
+\frac{\sigma}{\epsilon}\int_\Omega (W_+'(\varphi_h^m)+W_-'(\varphi^{m-1}))\frac{\varphi_h^m-\varphi^{m-1}}{\tau}\,dx\\
+r\int_{\partial\Omega} B_h^m\frac{\varphi_h^m-\varphi^{m-1}}{\tau}\,ds+\int_{\partial\Omega}(\gamma_+'(\varphi_h^m)+\gamma_-'(\varphi^{m-1}))\frac{\varphi_h^m-\varphi^{m-1}}{\tau}\,ds=0.
\end{aligned}$$

Using convexity and concavity of W_+ and W_-, and γ_+ and γ_- it holds

$$\begin{aligned}
\int_\Omega (W_+'(\varphi_h^m)+W_-'(\varphi^{m-1}))\frac{\varphi_h^m-\varphi^{m-1}}{\tau}\,dx\geq\frac{1}{\tau}\int_\Omega W(\varphi_h^m)-W(\varphi^{m-1})\,dx,\\
\int_\Omega (\gamma_+'(\varphi_h^m)+\gamma_-'(\varphi^{m-1}))\frac{\varphi_h^m-\varphi^{m-1}}{\tau}\,ds\geq\frac{1}{\tau}\int_\Omega \gamma(\varphi_h^m)-\gamma(\varphi^{m-1})\,ds.
\end{aligned}$$

Summing up and using $v\cdot\nu_\Omega=0$, we obtain the desired result. □

Remark 8 (Adaptive meshing)**.** *In general, in diffuse interface simulations it is advantageous to use adaptive meshes to resolve the interfacial region. Then in every time step additional prolongation operators between subsequent meshes are required. As a consequence, in this case the energy inequality from Theorem 7 only holds with the prolongated data for the energy from the old time instance. We further note that special care has to be taken for prolongating the velocity field, as the prolongated velocity field typically is not solenoidal with respect to the new mesh. We refer to [9, 36] for further discussion of this topic.*

3.1. Variants

Let us state variants of the above discretization scheme (16)–(19) for numerical comparison. We note, that (16)–(19) is a fully coupled and non-linear scheme.

3.1.1. A stable decoupled scheme

If $r\equiv 0$ the scheme is only coupled by the transport term $(\varphi^{m-1}v_h^m,\nabla\Psi)$ in (18). The same holds for $l\to\infty$, which results in the commonly used no-slip condition for the Navier–Stokes equation. In the case of no-slip conditions B is independent of v and thus again the only coupling is the transport term in (18).

In both cases we can decouple the Navier–Stokes equation and the Cahn–Hilliard equation by using an augmented velocity field in (18), see for example [11, 13, 18, 37]. Here we substitute $-\int_\Omega \varphi^{m-1} v_h^m \cdot \nabla \Psi \, dx$ in (18) by

$$-\int_\Omega \varphi^{m-1} v^{m-1} \cdot \nabla \Psi \, dx + \tau \int_\Omega (\rho^{m-1})^{-1} |\varphi^{m-1}|^2 \nabla \mu_h^m \cdot \nabla \Psi \, dx. \tag{20}$$

The resulting scheme is decoupled; we can first solve (18) and (19) and thereafter (16) and (17). This scheme is also energy stable, as the additional integral compensates terms arising from Hölder's and Young's inequality to balance the first integral with the numerical dissipation $\frac{1}{2}\int_\Omega \rho^{m-1}|v_h^m - v^{m-1}|^2 \, dx$. This scheme with no-slip conditions for Navier–Stokes and $r \equiv 0$ is analyzed in [11] for different treatments of W'. We also refer to [38] for an alternative decoupling in the case of constant density. Here the systems are decoupled by using v^{m-1} in (18), and the energy stability is obtained by introducing a step size restriction for the temporal discretization.

If $r > 0$, we use v^{m-1} in the definition of B_h^m in (19) and v_h^m in the corresponding term in (16) and can still derive an energy inequality containing an error of order $r\int_{\partial\Omega}(v_h^m - v^{m-1}) \cdot \nabla \varphi^{m-1} \, ds$. In [11] a no-slip condition is assumed for v to decouple the boundary conditions. Then the decoupling proposed in (20) is sufficient to decouple the Navier–Stokes and the Cahn–Hilliard equation.

We note that this scheme can be applied for any bulk energy potential that admits a convex-concave splitting.

3.1.2. A stable decoupled and linear scheme

Using the decoupling proposed in Section 3.1.1, the only nonlinearity in the scheme arises from W_+'. In [16–18], a stabilized linear scheme is used and the term $W_+'(\varphi_h^m) + W_-'(\varphi^{m-1})$ is substituted by $W'(\varphi^{m-1}) + S_W(\varphi_h^m - \varphi^{m-1})$, where S_W is a suitable stabilization parameter. For smooth W it satisfies $S_W \geq \frac{1}{2}\max_t |W''(t)|$. It can be derived by Taylor expansion of W at φ^{m-1}, see for example [16]. As W^s is of class $C^{1,1}$ only, $(W^s)''$ jumps at ξ^{-1} from $-\xi^2$ to $(s-1)\xi^2$. In this case we use $S_W \geq s/2$. For large values of s we expect that this stabilization will prevent changes in φ and thus might have a deep impact on the allover dynamics. This is investigated in Section 4 and especially discussed in Remark 11. To linearize γ we substitute $\gamma_+'(\varphi_h^m) + \gamma_-'(\varphi^{m-1})$ by $\gamma'(\varphi^{m-1}) + S_\gamma(\varphi_h^m - \varphi^{m-1})$ with $S_\gamma \geq \frac{1}{2}\max_t |\gamma''(t)|$ and especially $S_\gamma \geq \frac{1}{2}\sigma_{12}|\cos(\theta_s)|$ in the case of γ^{cc}. Here, again S_γ is obtained by Taylor expansion of γ at φ^{m-1}.

Remark 9 (Further schemes)**.** *For further discretization schemes of the bulk energy density W we refer for example to [11, 30, 33]. Second order schemes for the Cahn–Hilliard equation are for example proposed and analyzed in [30, 33, 39–41]. Recently the Invariant Energy Quadratization approach for $W \equiv W^{poly}$ was proposed in [42]. It is used in [43] for the Cahn–Hilliard moving contact line model together with a Crank–Nicolson and a BDF2 scheme in time. However, typically for these schemes either higher regularity than W^s provides*

is required for W, or the particular W^{poly} is assumed and necessary. Moreover, unconditional energy stability is typically not proven yet.

Remark 10 (Energy Consistency)**.** *Considering the energy inequality from Theorem 7, the terms in the first line correspond to the discrete energy of the system, while the second line corresponds to the energy dissipation of the system, and the third line corresponds to numerical dissipation of the scheme. Based on this we can define four different values to define the energies in our system. These are the energy E^m at time instance m, the physical dissipation Δ_p^m at time instance m, the energy E_g^m introduced from gravity at time instance m, and the numerical dissipation Δ_n^m at time instance m. They are defined by*

$$E^m := \frac{1}{2}\int_\Omega \rho^m |v_h^m|^2 \, dx + \sigma \int_\Omega \frac{\epsilon}{2}|\nabla \varphi_h^m|^2 + \frac{1}{\epsilon} W(\varphi_h^m)\, dx + \int_{\partial\Omega} \gamma(\varphi_h^m)\, ds, \quad (21)$$

$$\begin{aligned}\Delta_p^m := {} & \tau \int_\Omega 2\eta^{m-1} |Dv_h^m|^2 \, dx + \tau \int_\Omega b |\nabla \mu_h^m|^2 \, dx \\ & + \tau \int_{\partial\Omega} l(\varphi^{m-1}) |v_{h,tan}^m|^2 \, ds + \tau \int_{\partial\Omega} r |B_h^m|^2 \, ds, \end{aligned} \quad (22)$$

$$E_g^m := \tau \int_\Omega \rho^{m-1} g \cdot v_h^m \, dx, \quad (23)$$

$$\Delta_n^m := E^{m-1} + E_g^m - E^m - \Delta_p^m. \quad (24)$$

We call a scheme thermodynamically consistent if Theorem 7 is fulfilled without the explicit form of the numerical dissipation, thus if

$$E^m + \Delta_p^m \leq E^{m-1} + E_g^m \quad (25)$$

holds, i.e., $\Delta_n^m \geq 0$. We investigate this energy inequality numerically in Section 4.

4. Numerics

In this section we numerically investigate the three schemes under consideration. In Section 4.1 we briefly give results from the well-known second benchmark in [32], where no contact line motion is included, to estimate the difference of the schemes in the bulk. In Section 4.2 we thereafter investigate the behavior of the contact line for a gravity-driven droplet sliding on an inclined surface in a two-dimensional setting.

We implement the schemes in Python3 using FEniCS 2018.1.0 [44, 45]. For the solution of the arising nonlinear and linear systems and subsystems the software suite PETSc 3.8.4 [46–48] together with the direct linear solver MUMPS 5.1.1 [49, 50] are utilized. Note, that we do not apply any preconditioning or subiterations except for the Newton iterations.

4.1. Rising Bubble

At first, we discuss the accuracy of the proposed schemes without moving contact lines. Later on, this allows for an evaluation of the influence of the schemes on the moving contact line. We employ the quantitative benchmark case proposed in [32]. In [51] it is found, that three different diffuse interface approximations together with the polynomial potential W^{poly} agree well with the sharp interface results from [32]. In [9] the benchmark is used to compare to a phase field model with a relaxed double obstacle potential.

4.1.1. Setup

Table 1 lists the properties of our simulations, which correspond to the second benchmark case in [32]. For details on the setup we refer to the references above. Note, that σ_{12} denotes the physical surface tension, yielding $\sigma \approx 1.24$ for $W^{s=100}$, $\sigma \approx 1.22$ for $W^{s=10}$ and $\sigma \approx 2.07$ for W^{poly_2}. Following [32], we introduce a characteristic length scale $L = 2r_0$, where r_0 equals the initial radius of the bubble, and a characteristic velocity scale $U = \sqrt{Lg}$. To classify our simulations we indicate in Table 1 the dimensionless numbers Reynolds $Re = \frac{\rho_l U L}{\eta_l}$, Eötvös (or Bond) $Eo = \frac{\rho_l g L^2}{\sigma}$, Capillary $Ca = \frac{\eta_l U}{\sigma}$, Atwood $At = \frac{\rho_l - \rho_g}{\rho_l + \rho_g}$, Cahn $Cn = \frac{\epsilon}{L}$ and Péclet $Pe = \frac{LU\epsilon}{b\sigma}$, see [52].

We apply no-slip boundary conditions for the velocity on the top and bottom walls, free-slip on the left and symmetry at the centerline through the bubble at $x = 0.5$. Similar to [9], we set $b = 10^{-3}\epsilon$ and $\epsilon = 0.02$. The time discretization step is set to different values and the final time is $t = 3$. We initialize the simulations by solving the Cahn–Hilliard equations without convection until a steady state is reached. In total, we perform 7 distinct simulations using the three schemes from Section 3 with W^{poly2} and W^s with $s = 100$, and one additional simulation with $s = 10$ for the fully linear and stabilized scheme with W^s, see the first three columns in Table 2. To get an impression of the influence of the discretization parameters, we use different values for τ and h_{min}, see columns four and five in Table 2.

In [32] a set of benchmark parameters is used, that we define in the phase field setting as follows.

The center of mass is calculated using

$$(x_c, y_c) = \frac{\int_\Omega (x, y) \frac{1+\varphi}{2}\, dx}{\int_\Omega \frac{1+\varphi}{2}\, dx}\ , \tag{26}$$

where $\frac{1+\varphi}{2} = 1$ indicates the droplet.

We define the mean velocity in unit direction $a \in \mathbb{R}^2$ as

$$v_a = \frac{\int_\Omega v \cdot a \frac{1+\varphi}{2}\, dx}{\int_\Omega \frac{1+\varphi}{2}\, dx}\ . \tag{27}$$

If a denotes the unit vector in rising direction, this is called rising velocity v_r, while if a points in sliding direction, we call this value sliding velocity v_s.

σ_{12}	ρ_l	ρ_g	η_l	η_g	g_y	Re	Eo	Ca	At
1.96	1000	1	10	0.1	-0.98	35	125	3.5	0.99
ϵ	b					Cn	Pe		
2×10^{-2}	2×10^{-5}					0.04	178		

Table 1: Parameters used in the rising bubble simulations.

Finally we define the stretching of the interface as

$$c = \frac{c_W \int_\Omega (\frac{\epsilon}{2}|\nabla\varphi_0|^2 + \frac{1}{\epsilon}W(\varphi_0))\,dx}{c_W \int_\Omega (\frac{\epsilon}{2}|\nabla\varphi|^2 + \frac{1}{\epsilon}W(\varphi))\,dx}\ . \tag{28}$$

Here the denominator denotes an approximation to the length of the interface represented by φ, and the numerator denotes the same for the initial phase field φ_0. If φ_0 denotes a sphere, this is equivalent to the circularity as defined in [32] as the volume of the bubble is constant over time.

Remark 11 (Choice of s in W^s)**.** *For the choice of the relaxation parameter s in W^s, see Remark 2, several points must be considered. To reduce the intermixing between the phases and increase the rate at which the equilibrium profile of φ is reestablished after a deformation, it is desirable to exhibit a large spinodal region and subsequently a small metastable region [53]. The metastable region of the bulk energy potential W^s is located between $1 > |\varphi| > \xi^{-1} = 1 - \frac{1}{s}$, while the metastable region for W^{poly} is located between $1 > |\varphi| > \sqrt{3^{-1}} \approx 0.577$. Thus already for small values of s, say $s = 10$, the metastable region of W^s is significantly smaller than the metastable region of W^{poly}. Furthermore, referring to [9, 54], the value of s controls the deviation of the L^∞ norm of φ from 1. Since ρ and η directly depend on φ a small deviation is desirable, which is achieved by a large value of s.*

On the other hand, the stable decoupled and linear scheme, Section 3.1.2, includes a stabilization parameter S_W which has to be chosen like $S_W > s/2$ for W^s. In this case a large value of s has a severe impact on the overall dynamics as the stabilization can be interpreted as adding the quadratic potential $\frac{S_W}{2}\|\varphi - \varphi^{m-1}\|^2$ to W for given φ^{m-1}. For large values of S_W thus $\varphi \equiv \varphi^{m-1}$ is preferred. To show the influence of S_W in the case $W \equiv W^s$ we test the linear and decoupled scheme with two values of s.

4.1.2. Results

The resulting benchmark values are listed in Table 2. As it is not even clear in the sharp interface simulations whether or not topological changes develop, e.g. the separation of trailing gas filaments, we compare our results only up to time instance $t = 2$, see [51] . Our results show that all the schemes give very similar results compared to the sharp interface solution even for the significantly larger time step $\tau = 0.001$ and on a coarse mesh with $h_{min} = 0.0125$. In

general, decoupling the two systems has a very small impact on the benchmark values. For even larger $\tau = 0.008$ the coupled scheme is advantageous against the decoupled schemes. The latter might be explained by the fact, that the decoupling adds artificial diffusion of order τ to the Cahn–Hilliard system, see (20). Thus we expect a stronger influence of this decoupling for larger values of τ. As expected, the stabilized linear scheme together with $W^{s=100}$ hinders the dynamics of the rising bubble. However, the results improve significantly with smaller s. All schemes together with $W^{s=100}$ give slightly better results compared to W^{poly_2} except the decoupled/linear scheme. However, for very small τ and h_{min} the results converge towards similar values.

Concerning the computational effort the difference in using $W^{s=100}$ or W^{poly_2} is insignificant. The decoupled/nonlinear and decoupled/linear schemes are around 1.4 respectively 2.0 times faster than the coupled scheme. In the nonlinear schemes 2-3 Newton iterations are needed per time step. Note that the performance results strongly dependent on the solver and whether sophisticated preconditioning is applied. For an efficient preconditioner for the coupled/nonlinear system we refer to [55].

4.2. Sliding Droplet

To compare the influence of the numerical schemes from Section 3 on the moving contact line, we perform simulations of single droplets sliding down an inclined surface. Besides the effect of gravity on the droplet movement, this test case allows to observe both an advancing and receding contact line.

4.2.1. Setup

In Figure 1 the initial configuration is shown and Table 3 lists the properties of our simulations. The fluid properties are chosen to be similar to the first rising bubble test case in [32]. Note, that σ_{12} denotes the physical surface tension, yielding $\sigma \approx 15.58$ for $W^{s=100}$, $\sigma \approx 15.34$ for $W^{s=10}$ and $\sigma \approx 25.98$ for W^{poly_2}. A liquid droplet with radius $r_0 = 0.25$ is placed in a 0.5×2.0 rectangular domain at (0,1.5) on a smooth, solid surface with an initial contact angle of 90°. The inclination angle of the plate is 45°. The density of the droplet is greater than that of the surrounding fluid. We have no-slip boundary conditions for the velocity on the left and right side and free-slip on the top side. The conditions (6) and (7) are applied on the bottom solid surface, see Figure 1. The influence of the boundary conditions (6) and (7) on the sliding droplets are examined by varying the static contact angle θ, the relaxation factor r and the slip coefficient l, see the fifth to seventh column in Table 4. We vary the contact angle from super-hydrophilic (5°) to super-hydrophobic (150°) [56]. We initialize the simulations by solving the Cahn–Hilliard equations without convection and a contact angle of 90° until a steady state is reached.

In a first step, we compare 21 distinct simulations obtained with the three schemes from Section 3 with W^{poly_2} and W^s with $s = 100$, and one additional simulation with $s = 10$ for the fully linear and stabilized scheme with W^s, see the first two columns in Table 4. These simulation are performed with

Bulk pot.	Deco./Lin.?		τ	h_{min}	y_c	$v_{\max}$	$t_{v_{\max}}$	$c_{\min}$	$t_{c_{\min}}$
$W^{s=100}$	no/no	8	$\times 10^{-3}$	0.012 50	0.9024	0.2433	0.7520	0.6962	1.99
$W^{s=100}$	no/no	1	$\times 10^{-3}$	0.012 50	0.9071	0.2479	0.7410	0.6636	2.00
$W^{s=100}$	no/no	5	$\times 10^{-5}$	0.006 25	0.9059	0.2475	0.7349	0.6611	2.00
$W^{s=100}$	yes/no	8	$\times 10^{-3}$	0.012 50	0.8816	0.2486	0.7600	0.7124	1.99
$W^{s=100}$	yes/no	1	$\times 10^{-3}$	0.012 50	0.8994	0.2503	0.7460	0.6710	2.00
$W^{s=100}$	yes/no	5	$\times 10^{-5}$	0.006 25	0.9060	0.2479	0.7349	0.6614	2.00
$W^{s=100}$	yes/yes	8	$\times 10^{-3}$	0.012 50	0.7128	0.2066	1.9920	0.7355	1.99
$W^{s=100}$	yes/yes	1	$\times 10^{-3}$	0.012 50	0.8642	0.2374	0.8710	0.8290	2.00
$W^{s=100}$	yes/yes	5	$\times 10^{-5}$	0.006 25	0.8996	0.2457	0.7449	0.7455	2.00
$W^{s=10}$	yes/yes	8	$\times 10^{-3}$	0.012 50	0.8475	0.2370	0.8800	0.8154	1.99
$W^{s=10}$	yes/yes	1	$\times 10^{-3}$	0.012 50	0.8951	0.2402	0.7600	0.6965	2.00
$W^{s=10}$	yes/yes	5	$\times 10^{-5}$	0.006 25	0.9030	0.2472	0.7349	0.6725	2.00
W^{poly_2}	no/no	8	$\times 10^{-3}$	0.012 50	0.8826	0.2206	0.7680	0.6857	1.99
W^{poly_2}	no/no	1	$\times 10^{-3}$	0.012 50	0.8865	0.2249	0.7610	0.6618	2.00
W^{poly_2}	no/no	5	$\times 10^{-5}$	0.006 25	0.8941	0.2494	0.7517	0.6536	2.00
W^{poly_2}	yes/no	8	$\times 10^{-3}$	0.012 50	0.8668	0.2278	0.7760	0.7092	1.99
W^{poly_2}	yes/no	1	$\times 10^{-3}$	0.012 50	0.8815	0.2279	0.7680	0.6699	2.00
W^{poly_2}	yes/no	5	$\times 10^{-5}$	0.006 25	0.8944	0.2429	0.7649	0.6556	2.00
W^{poly2}	yes/yes	8	$\times 10^{-3}$	0.012 50	0.8646	0.2272	0.7840	0.7193	1.99
W^{poly_2}	yes/yes	1	$\times 10^{-3}$	0.012 50	0.8813	0.2278	0.7690	0.6713	2.00
W^{poly_2}	yes/yes	5	$\times 10^{-5}$	0.006 25	0.8944	0.2429	0.7649	0.6559	2.00
ref. diffuse		4	$\times 10^{-3}$		0.8994	0.2503	0.7960	0.6684	1.98
ref. sharp		1.95	$\times 10^{-4}$		0.9154	0.2502	0.7313	0.6901	2.00

Table 2: Benchmark values for the second benchmark proposed in [32]. Here y_c denotes the center of mass at time $t = 2$, $v_{\max}$ denotes the maximum rising velocity that appears at time $t_{v_{\max}}$, and $c_{\min}$ denotes the minimal circularity that appears at time $t_{c_{\min}}$. See (26)–(28) or [32] for the definition of these values. As reference we choose the results from the 3rd group participating in [32] (ref. sharp) and for model 3 in [51] (ref. diffuse, $\epsilon = 0.02$). We note that in the latter piece wise quadratic finite elements are used for φ and μ, which is the reason, why we do not provide a value for $h_{\min}$. Further, we do not provide a value for $h_{\min}$ for the reference solution in the sharp setting because here a different numerical approach is used, that can not directly be compared with the present situation.

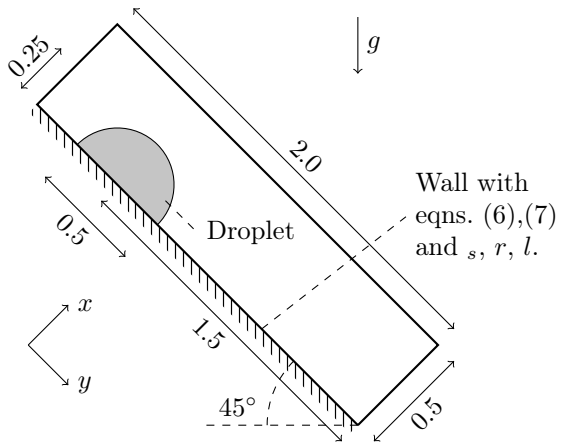

Figure 1: Initial configuration for the sliding droplet simulations.

σ_{12}	ρ_l	ρ_g	η_l	η_g	g	Re	Eo	Ca	At
24.5	1000	100	10	1	-0.98	35	10	0.28	0.81
ϵ	b					Cn	Pe		
2×10^{-2}	2×10^{-5}					0.04	14		

Table 3: Parameters used in the sliding droplet simulations.

a relatively coarse mesh ($h_{min} = 0.0125$) and large time step ($\tau = 0.001$) to discuss the practical applicability of the solution schemes. Afterwards, we show the thermodynamic consistency of the schemes and compare the physical and numerical dissipation rates. To discuss the influence of the time step size on the results, we perform 14 additional simulations with τ between 0.008 and 0.00025. Finally, we perform 8 simulations with varying interfacial thicknesses ϵ on a very fine mesh ($h_{min} = 0.0002$) to briefly discuss the convergence to the sharp-interface limit.

Remark 12 (Choice of r and l)**.** *For meaningful values of the relaxation parameter r and the slip coefficient l, we write* (6) *and* (7) *in non-dimensionalized form,*

$$\left[\frac{Ca}{Cn} 2\hat{\eta} D\hat{v}\nu_\Omega + \frac{Ca}{Cn}\frac{L}{l_s} - \hat{L}\hat{\nabla}\varphi\right] \times \nu_\Omega = 0, \tag{29}$$

$$\frac{Ca}{Cn}\frac{r_s}{L}(\partial_{\hat{t}}\hat{\varphi} + \hat{v}\hat{\nabla}\varphi) + \hat{L} = 0, \tag{30}$$

in which $Ca = \eta_l U/\sigma$ and $Cn = \epsilon/L$ are the Capillary number respectively the Cahn number, and L and U are some characteristic macroscopic length scale respectively velocity. We choose $r = r_s\eta_l$ and $l = \eta_l/l_s$ such that the dimensionless groups $\frac{Ca}{Cn}\frac{L}{l_s}$ and $\frac{Ca}{Cn}\frac{r_s}{L}$ are of $\mathcal{O}(1)$, see [57].

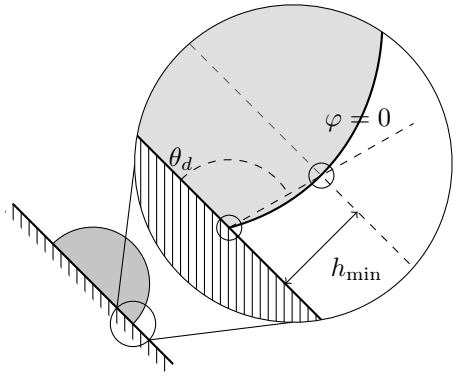

Figure 2: Measurement of the dynamic (or apparent) contact angle.

As benchmark values we again use the three values defined in Section 4.1 with minor modifications. For the center of mass, we use a coordinate system that is aligned with the inclined plate, see Figure 1, and for the now called sliding velocity, we use for a the unit vector in tangential direction to the inclined plate. The stretching of the interface is defined as before.

Additionally, we evaluate two values that are specific for the moving contact line setup. For both the receding and advancing contact line the position of the contact points and a dynamic (or apparent) contact angle measured at some height above the contact points are evaluated. The position of a contact point is defined by

$$y_p = y \text{ on } \partial\Omega \text{ where } \varphi = 0 \,, \tag{31}$$

and the dynamic contact angle θ_d is calculated by linear interpolation between y_p and the intersection $y_{p+\Delta}$ where $\varphi = 0$ and $\Delta = h_{\min}$, see Figure 2 and [58].

4.2.2. Results

Comparison of droplet shapes and characteristic values obtained on a coarse mesh and with a large time step. In dependence on θ_s, r and l the droplets show characteristic developments. The calculated shapes for different combinations of θ_s, r and l at $t = 0.0; 0.5; 1.0; 1.5; 2.0$ are presented in Figure 3. All the simulated droplets show the expected physical behavior: on the hydrophobic surface (third row) the droplet contracts, whereas the droplets spread on the hydrophilic surface (second row). In addition, the droplets slide down the surface due to the density difference and gravity. The different behavior at the advancing and receding contact points is visible and one can observe nonequilibrium contact angles in the second and third row. It is evident that there are virtually no differences between the coupled (solid black) and decoupled schemes (crosses) for all contact angles. In contrast, in the linearized scheme with $s = 100$ (dashed black) the dynamics are greatly reduced. Similar as in the rising bubble case, a smaller s ($s = 10$, dashed gray) leads to improvements.

For comparison, we show the behavior of the droplet with the coupled scheme and W^{poly_2} (dotted line). Here, a slightly different droplet shape is observed especially for later times and large contact angles.

The evolution of the slide velocity v_s, the position of the contact points y_p along the surface and the dynamic contact angle θ_d are displayed in Figure 4. Again, we show all the schemes together with $W^{s=100}$ and in addition the stabilized scheme together with $W^{s=10}$ and the coupled, nonlinear scheme with W^{poly_2}. To allow for a more quantitative comparison between the solution schemes, we list the characteristic values at $t = 2$ in Table 4. As expected, in simulations without equilibrium contact angle relaxation ($r = 0$) and slip ($l = 1e6$) (first row) the apparent contact angles on both sides of the droplets stay near the equilibrium value $\theta_s = 90°$ the whole time. In contrast, applying the full boundary conditions (6) and (7) with $r = 0.35$ and $l = 140$ leads to clearly visible advancing and receding contact angles (third column). As before, no difference is visible between the coupled (solid black) and decoupled (black crosses) nonlinear schemes for all the characteristic quantities. The characteristic values at $t = 2$ differ only very slightly. The results with the decoupled, stabilized scheme with $s = 100$ (dashed black) are very far off and show very low sliding velocities (left column) and a different contact point behavior (middle column), especially for $\theta_s = 150°$ (last row). The sliding velocities at $t = 2$ differ greatly. In contrast to the comparison in the bulk only, see Section 4.1, the usage of the coupled scheme with W^{poly_2} (dotted black) gives results which are noticeable different from the results with $W^{s=100}$. This is most obvious in the simulations with $\theta_s = 5°$ (middle row): the sliding velocity (left column) is slower and the terminal velocity is reached later. In addition, the receding and advancing contact angles are both lower than in the simulations with $W^{s=100}$. For example, at $t = 2$, the advancing contact angle for W^{poly_2} is around 12° smaller than in the nonlinear simulations with $W^{s=100}$.

Thermodynamic consistency and comparison of dissipation rates. We reveal the thermodynamic consistency of the schemes by calculating the evolution of the energy inequality using (25). We use γ^{cc} and set $\theta_s = 150°$, $r = 0.35$ and $l = 140$. We observe, that Δ_n^m is positive for all times, which justifies that the schemes are thermodynamically consistent, see (25). Note that for $r > 0$ we introduce an additional error as soon as we use the decoupling strategy. We observe, that the physical dissipation for the three nonlinear schemes are close together, while the physical dissipation for the linear model is strongly reduced. This corresponds to the reduced dynamics that are observed in Figure 3 for the linear schemes, especially for $s = 100$. This influence can be reduced by using very small time steps and finer meshes, see the results for the rising bubble case in Table 2. Comparing the numerical and physical dissipation of the nonlinear schemes, Δ_n^m only accounts for around 25% of the total dissipation even for large time steps. Furthermore, by halving the time step τ, the numerical dissipation Δ_n^m relative to the total dissipation $\Delta_n^m + \Delta_p^m$ is greatly reduced to around 12%, see the grey plots in the bottom figure of Figure 5.

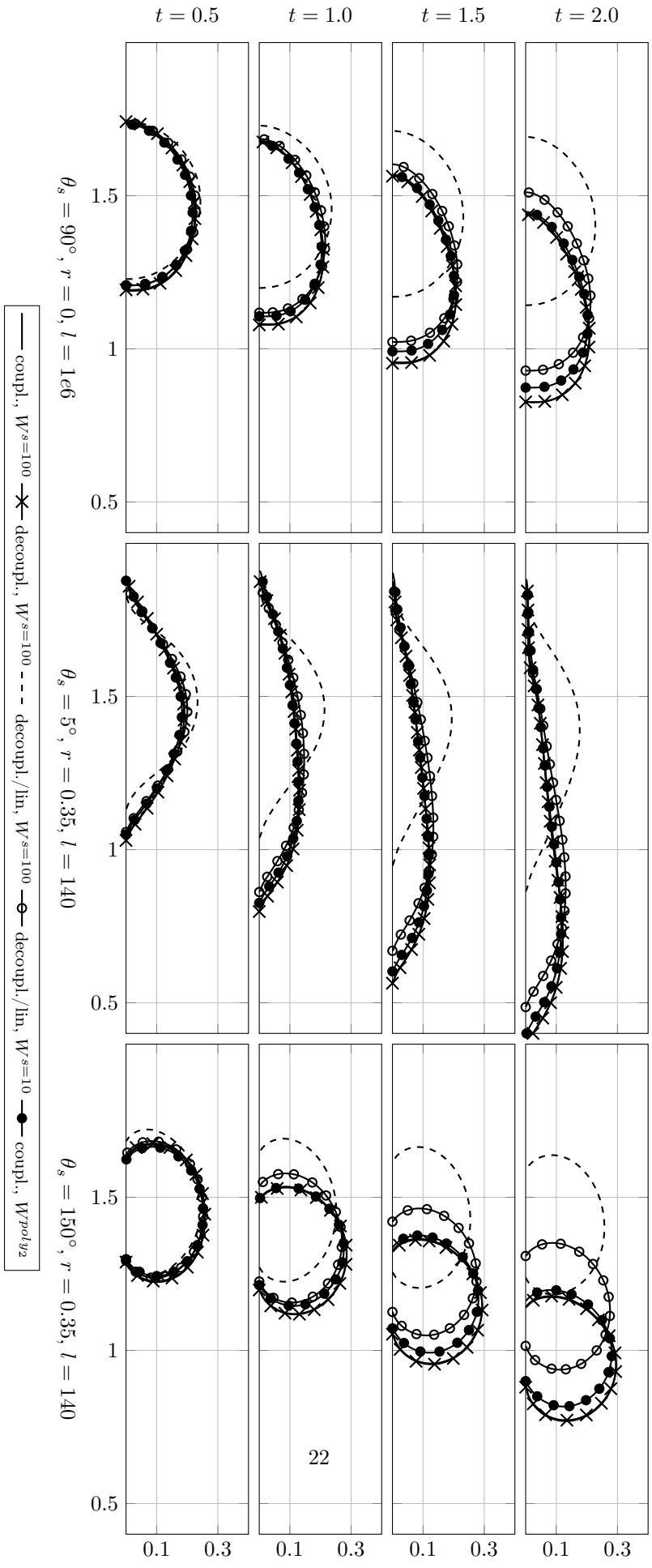

Figure 3: Shapes of the sliding droplets calculated with the schemes from Section 3. Three different surfaces ranging from superhydrophilic (5°, middle) to superhydrophobic (150°, bottom) are compared. The corresponding parameters can be found in Tables 3 and 4.

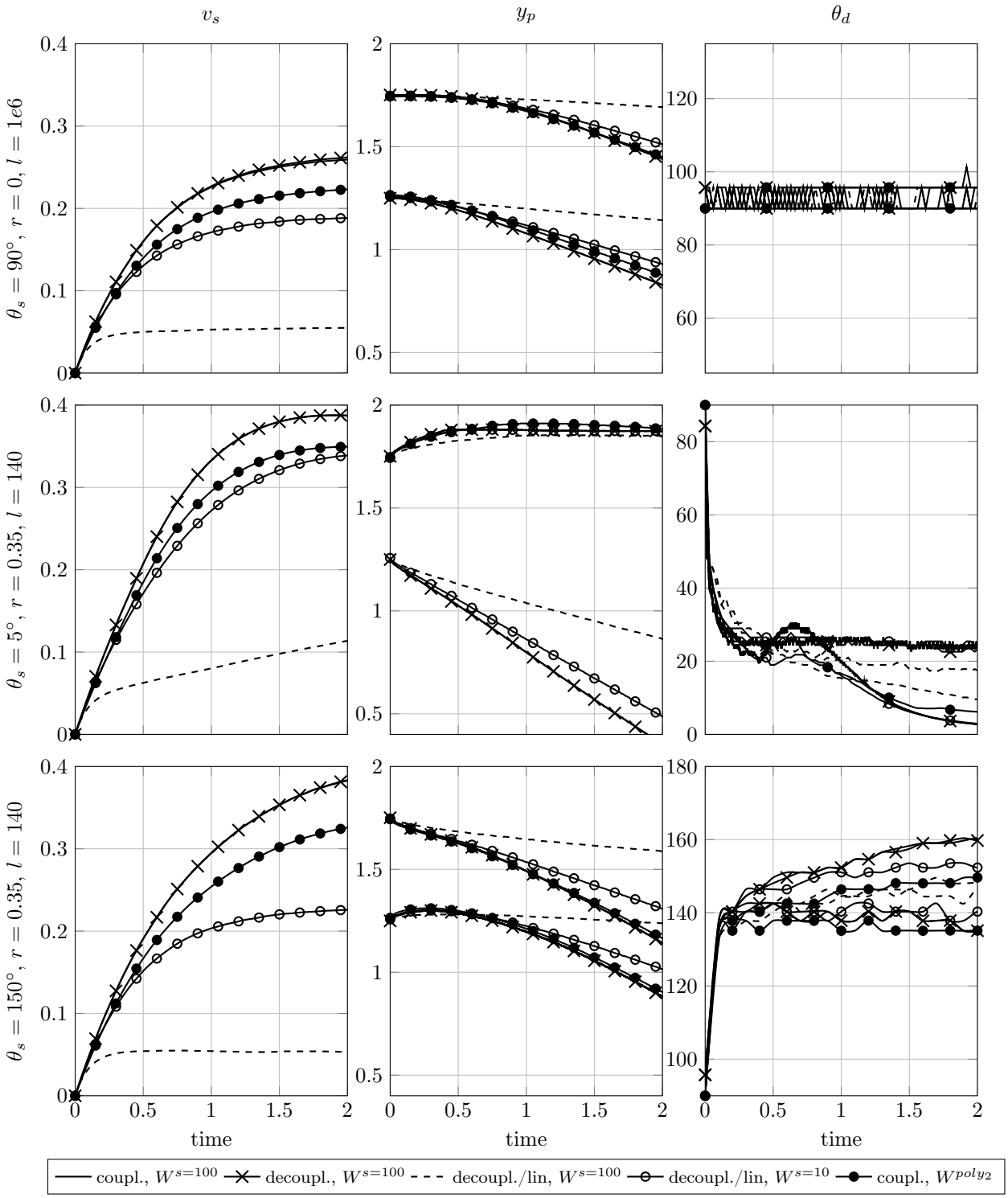

Figure 4: Characteristic quantities calculated with the schemes from Section 3. Three different surfaces ranging from super-hydrophilic (5°, middle) to super-hydrophobic (150°, bottom) are compared. The corresponding parameters can be found in Tables 3 and 4

Bulk pot.	Deco./Lin.?	τ	h	θ	r	l	y_c	$y_{p,a}$	$y_{p,r}$	v_s	c	$\theta_{d,a}$	$\theta_{d,r}$
$W^{s=100}$	no/no						1.1067	0.8298	1.4442	0.2593	0.9550	96	96
$W^{s=100}$	yes/no						1.1048	0.8279	1.4398	0.2619	0.9570	90	96
$W^{s=100}$	yes/yes						1.4087	1.1426	1.6926	0.0549	0.9921	90	96
$W^{s=10}$	yes/yes	0.001	0.0125	90	0	1000000	1.1904	0.9302	1.5115	0.1883	0.9723	90	96
W^{poly_2}	no/no						1.1390	0.8765	1.4500	0.2231	0.9667	90	96
W^{poly_2}	yes/no						1.1369	0.8757	1.4469	0.2239	0.9685	90	96
W^{poly2}	yes/yes						1.1437	0.8842	1.4548	0.2184	0.9696	90	96
$W^{s=100}$	no/no						0.9745	0.8818	1.1438	0.3829	0.8905	160	135
$W^{s=100}$	yes/no						0.9749	0.8818	1.1438	0.3833	0.8906	160	135
$W^{s=100}$	yes/yes						1.4053	1.2375	1.5876	0.0535	0.9368	148	146
$W^{s=10}$	yes/yes	0.001	0.0125	150	0.35	140	1.1340	1.0154	1.3091	0.2259	0.9149	154	140
W^{poly_2}	no/no						1.0263	0.9030	1.1651	0.3257	0.9066	148	135
W^{poly2}	yes/no						1.0266	0.9046	1.1660	0.3236	0.9069	148	132
W^{poly_2}	yes/yes						1.0410	0.9185	1.1823	0.3092	0.9093	148	135
$W^{s=100}$	no/no						0.9330	0.3551	1.8732	0.3872	0.5286	24	3
$W^{s=100}$	yes/no						0.9331	0.3534	1.8736	0.3874	0.5282	24	3
$W^{s=100}$	yes/yes						1.3550	0.8641	1.8510	0.1137	0.7592	17	10
$W^{s=10}$	yes/yes	0.001	0.0125	5	0.35	140	1.0188	0.4872	1.8750	0.3389	0.5726	24	3
W^{poly2}	no/no						0.9763	0.3253	1.8850	0.3494	0.5264	6	3
W^{poly2}	yes/no						0.9736	0.3252	1.8865	0.3527	0.5244	6	3
W^{poly2}	yes/yes						0.9808	0.3251	1.8849	0.3492	0.5318	6	3

Table 4: Parameters and characteristic values for the sliding droplets simulations. For y_c and c see caption of Table 2. In addition, y_p and θ_d denote the position of the contact points and the dynamic contact angles. The first and second values correspond to the advancing and receding contact point respectively angle. The slide velocity is v_s and all values are reported at $t = 2$.

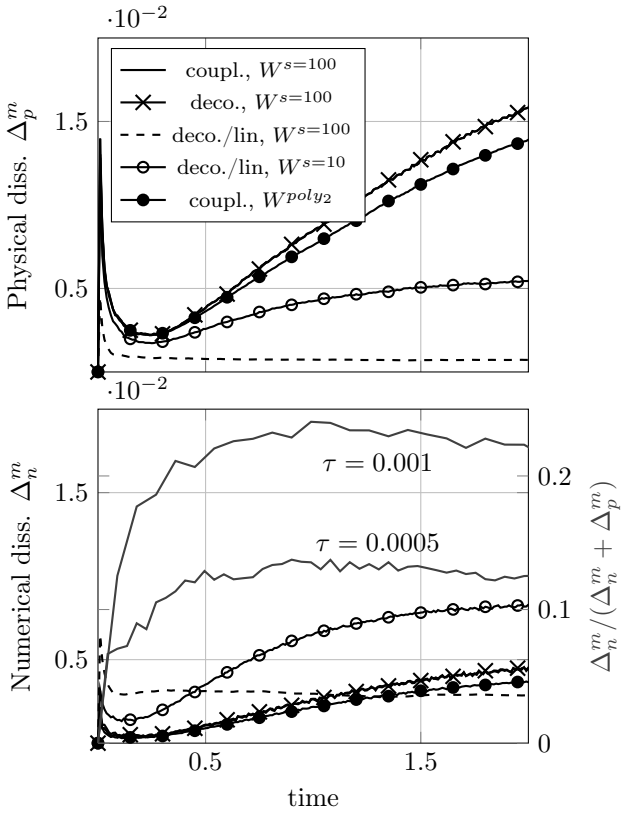

Figure 5: Validity of the energy inequality (25) (bottom) and the physical dissipation (22) (top) for the different schemes. All simulations are performed with $\tau = 0.001$, $h_{min} = 0.0125$, $\theta_s = 150°$, $r = 0.35$ and $l = 140$. The coupled/nonlinear and decoupled/nonlinear scheme match almost perfectly and appear as a single graph. The numerical dissipation relative to the total dissipation is shown for two different time steps sizes in the bottom figure.

Comparison of characteristic values obtained with smaller time steps τ. We show the behavior of the schemes for different time step sizes in Table 5. For small time steps, both the nonlinear schemes (coupled and decoupled) converge to the same characteristic values for the particular bulk energy potentials. However, by comparing the values between the different bulk energy potentials, we note, that the differences are still relatively large even for small time steps. Again, the linear scheme together with W^s gives results far away from the solution obtained with the coupled schemes.

Convergence to sharp-interface limit. In Table 6 we show solutions obtained with both bulk energy potentials and smaller ϵ on a very fine mesh ($h_{min} = 0.0002$). To reduce the computational effort, the inclination angle of the plate, see Figure 1, is set to zero and the simulation is already stopped at $t = 0.2$. As expected for $b = \mathcal{O}(\epsilon)$ and $r = \mathcal{O}(1)$, see [29], the rate of convergence for

Bulk pot.	Deco./Lin.?	τ	y_c	$y_{p,a}$	$y_{p,r}$	v_s	c	$\theta_{d,a}$	$\theta_{d,r}$
$W^{s=100}$	no/no	8×10^{-3}	1.1872	1.0606	1.3681	0.1926	0.9172	158	135
$W^{s=100}$	no/no	1×10^{-3}	0.9745	0.8818	1.1438	0.3829	0.8905	160	135
$W^{s=100}$	no/no	2.5×10^{-4}	0.9382	0.8539	1.1025	0.4186	0.8818	160	138
$W^{s=100}$	yes/no	8×10^{-3}	1.1913	1.0637	1.3687	0.1965	0.9169	157	138
$W^{s=100}$	yes/no	1×10^{-3}	0.9749	0.8818	1.1438	0.3833	0.8906	160	135
$W^{s=100}$	yes/no	2.5×10^{-4}	0.9383	0.8539	1.1025	0.4187	0.8818	160	138
$W^{s=100}$	yes/yes	8×10^{-3}	1.4833	1.2785	1.6958	0.0198	0.9657	140	140
$W^{s=100}$	yes/yes	1×10^{-3}	1.4053	1.2375	1.5876	0.0535	0.9368	148	146
$W^{s=100}$	yes/yes	2.5×10^{-4}	1.2442	1.1002	1.4177	0.1498	0.9251	152	140
$W^{s=10}$	yes/yes	8×10^{-3}	1.3802	1.2484	1.5842	0.0574	0.9297	148	142
$W^{s=10}$	yes/yes	1×10^{-3}	1.1340	1.0154	1.3091	0.2259	0.9149	154	140
$W^{s=10}$	yes/yes	2.5×10^{-4}	1.0011	0.9009	1.1648	0.3499	0.8966	157	138
W^{poly2}	no/no	8×10^{-3}	1.2590	1.0789	1.3748	0.1663	0.9266	146	135
W^{poly2}	no/no	1×10^{-3}	1.0263	0.9030	1.1651	0.3257	0.9066	148	135
W^{poly2}	no/no	2.5×10^{-4}	0.9956	0.8748	1.1268	0.3564	0.8995	150	135
W^{poly2}	yes/no	8×10^{-3}	1.1909	1.0895	1.3766	0.1630	0.9259	146	138
W^{poly2}	yes/no	1×10^{-3}	1.0266	0.9046	1.1660	0.3236	0.9069	148	132
W^{poly2}	yes/no	2.5×10^{-4}	0.9958	0.8748	1.1255	0.3558	0.8995	150	138
W^{poly2}	yes/yes	8×10^{-3}	1.2285	1.1302	1.4226	0.1339	0.9284	146	135
W^{poly2}	yes/yes	1×10^{-3}	1.0410	0.9185	1.1823	0.3092	0.9093	148	135
W^{poly2}	yes/yes	2.5×10^{-4}	1.0000	0.8786	1.1318	0.3517	0.9007	150	135

Table 5: Characteristic values for the sliding droplet simulations obtained with different values of τ ($h_{min} = 0.0125$, $\theta = 150°$, $r = 0.35$, $l = 140$). For details about the setup and the characteristic values see the caption of Table 4.

Bulk pot.	ϵ	b	y_p
$W^{s=100}$	0.040	4×10^{-5}	0.1887
$W^{s=100}$	0.020	2×10^{-5}	0.1987
$W^{s=100}$	0.010	1×10^{-5}	0.2032
$W^{s=100}$	0.005	5×10^{-6}	0.2112
W^{poly_2}	0.040	4×10^{-5}	0.1902
W^{poly_2}	0.020	2×10^{-5}	0.1977
W^{poly_2}	0.010	1×10^{-5}	0.2027
W^{poly_2}	0.005	5×10^{-6}	0.2097

Table 6: Position of the contact line for a receding droplet (similar to the sliding droplet case with inclination angle set to zero) obtained with different values of ϵ on a very fine mesh $h_{min} = 0.0002$ ($\tau = 0.001$, $\theta = 150°$, $r = 0.35$, $l = 140$). The decoupled/nonlinear solution scheme is used. For details about the setup and the characteristic values see the caption of Table 4.

both potentials is very slow and the sharp-interface limit is not reached yet. However, from our simulations we can conclude, that on the fine mesh both potentials give very similar results and exbibit the same behavior for smaller ϵ. For larger ϵ, solutions obtained with $W^{s=100}$ seem to diverge slightly faster from the sharp-interface solution than solutions obtained with W^{poly_2}.

5. Conclusion

We compare the quality of the numerical results with three different schemes and two different bulk energy potentials. For simulations without a moving contact line (rising bubble case), we find very similar results in the bulk independent of the coupling and linearization for both potentials. However, the linearization of W^s for large s hinders the dynamics to a great extend but gets better for smaller s. For the simulations including moving contact lines (sliding droplet case), the differences between the polynomial potential W^{poly_2} and the relaxed double-obstacle potential W^s are more pronounced. Again, we observe a strong truncation of the allover dynamics using W^s together with the linear scheme. In both cases, the influence of the decoupling of the Navier–Stokes and Cahn–Hilliard system slightly depends on the time step size. However, the decoupling has a negligible influence on the all-over dynamics even for larger time steps. Concerning the two tested bulk energy potentials, we observe, that both give in general physically sound results, but differences are still exists even for small time steps. The results and the behavior for smaller ϵ on a fine mesh are almost the same for both potentials. For larger ϵ, solutions obtained with $W^{s=100}$ seem to diverge slightly faster from a sharp-interface solution than with W^{poly_2}.

Summarizing our results, we find that

- the decoupling strategy gives excellent results while the computational effort is significantly reduced compared to the fully coupled scheme,

- a further linearization of the Cahn–Hilliard system applying the stabilization is not recommended together with W^s for large values of s,
- both bulk energy potentials produce sound and similar results in particular for a smaller interfacial thickness ϵ.

To further judge whether one of the potentials lead to more accurate results, high fidelity sharp interface results on flows with moving contact lines (similar to the benchmark performed in [32]) are critical. It is our hope, that the presented work sparks further comparisons of diffuse and sharp interface models especially for the frequently observed and relevant case of sliding droplets.

Acknowledgment

The authors thank Marion Dziwnik for helpful discussions on the scaling of the contact line surface tensions.

References

[1] D. Bonn, J. Eggers, J. Indekeu, J. Meunier, E. Rolley, Wetting and spreading, Rev. Mod. Phys. 81 (2) (2009) 739–805 (may 2009). doi:10.1103/RevModPhys.81.739.

[2] J. H. Snoeijer, B. Andreotti, Moving Contact Lines: Scales, Regimes, and Dynamical Transitions, Annu. Rev. Fluid Mech. 45 (1) (2013) 269–292 (jan 2013). doi:10.1146/annurev-fluid-011212-140734.

[3] D. Jacqmin, Contact-line dynamics of a diffuse fluid interface, J. Fluid Mech. 402 (2000) (2000) S0022112099006874 (jan 2000). doi:10.1017/S0022112099006874.

[4] D. M. Anderson, G. B. McFadden, A. A. Wheeler, Diffuse-interface methods in fluid mechanics, Annu. Rev. Fluid Mech. 30 (1) (1998) 139–165 (jan 1998). doi:10.1146/annurev.fluid.30.1.139.

[5] A. Carlson, G. Bellani, G. Amberg, Universality in dynamic wetting dominated by contact-line friction, Phys. Rev. E - Stat. Nonlinear, Soft Matter Phys. 85 (4) (2012) 1–5 (2012). arXiv:1111.1214, doi:10.1103/PhysRevE.85.045302.

[6] A. Eddi, K. G. Winkels, J. H. Snoeijer, Short time dynamics of viscous drop spreading, Phys. Fluids 25 (1) (2013). arXiv:1209.6150, doi:10.1063/1.4788693.

[7] T. Qian, X.-P. Wang, P. Sheng, A variational approach to moving contact line hydrodynamics, Journal of Fluid Mechanics 564 (2006) 333–360 (2006).

[8] H. Abels, H. Garcke, G. Grün, Thermodynamically consistent, frame indifferent diffuse interface models for incompressible two-phase flows with different densities, Mathematical Models and Methods in Applied Sciences 22 (3) (2012) 1150013(40) (March 2012). doi:10.1142/S0218202511500138.

[9] H. Garcke, M. Hinze, C. Kahle, A stable and linear time discretization for a thermodynamically consistent model for two-phase incompressible flow, Applied Numerical Mathematics 99 (2016) 151–171 (January 2016).

[10] G. Grün, F. Klingbeil, Two-phase flow with mass density contrast: Stable schemes for a thermodynamic consistent and frame indifferent diffuse interface model, Journal of Computational Physics 257 (A) (2014) 708–725 (January 2014).

[11] G. Grün, F. Guillén-Gonzáles, S. Metzger, On Fully Decoupled Convergent Schemes for Diffuse Interface Models for Two-Phase Flow with General Mass Densities, Communications in Computational Physics 19 (5) (2016) 1473–1502 (May 2016). doi:10.4208/cicp.scpde14.39s.

[12] S. Aland, Time integration for diffuse interface models for two-phase flow, Journal of Computational Physics 262 (2014) 58–71 (April 2014). doi:10.1016/j.jcp.2013.12.055.

[13] F. Guillén-Gonzáles, G. Tierra, Splitting schemes for a Navier–Stokes–Cahn–Hilliard model for two fluids with different densities, Journal of Computational Mathematics 32 (6) (2014) 643–664 (2014). doi:10.4208/jcm.1405-m4410.

[14] Q. He, R. Glowinski, X.-P. Wang, A least-squares/finite element method for the numerical solution of the Navier–Stokes–Cahn–Hilliard system modeling the motion of the contact line, Journal of Computational Physics 230 (12) (2011) 4991–5009 (2011). doi:10.1016/j.jcp.2011.03.022.

[15] M. Gao, X.-P. Wang, A gradient stable scheme for a phase field model for the moving contact line problem, Journal of Computational Physics 231 (4) (2012) 1372 – 1386 (2012). doi:https://doi.org/10.1016/j.jcp.2011.10.015.

[16] J. Shen, X. Yang, H. Yu, Efficient energy stable numerical schemes for a phase field moving contact line model, Journal of Computational Physics 284 (2015) 617–630 (2015). doi:10.1016/j.jcp.2014.12.046.

[17] S. Aland, F. Chen, An efficient and energy stable scheme for a phase-field model for the moving contact line problem, International Journal for Numerical Methods in Fluids 81 (2016) 657–671 (2016). doi:10.1002/fld.4200.

[18] H. Yu, X. Yang, Numerical approximations for a phase-field moving contact line model with variable densities and viscosities, Journal of Computational Physics (334) (2017) 665–686 (2017).

[19] J. Shen, X. Yang, A Phase-Field Model and its Numerical Approximation for Two-Phase Incompressible Flows with Different Densities and Viscosities, SIAM Journal on Scientific Computing 32 (3) (2010) 1159–1179 (2010).

[20] M. Hintermüller, M. Hinze, M. H. Tber, An adaptive finite element Moreau–Yosida-based solver for a non-smooth Cahn–Hilliard problem, Optimization Methods and Software 26 (4-5) (2011) 777–811 (2011). doi:10.1080/10556788.2010.549230.

[21] S. Aland, A. Hahn, C. Kahle, R. Nürnberg, Comparative Simulations of Taylor Flow with Surfactants Based on Sharp- and Diffuse-Interface Methods, Springer International Publishing, Cham, 2017, pp. 639–661 (2017). doi:10.1007/978-3-319-56602-3_22.

[22] H. Abels, D. Breit, Weak Solutions for a Non-Newtonian Diffuse Interface Model with Different Densities, Nonlinearity 29 (2016) 3426–3453 (2016). doi:10.1088/0951-7715/29/11/3426.

[23] L. Caffarelli, N. Muler, An L^∞ Bound for Solutions of the Cahn–Hilliard Equation, Archive for Rational Mechanics and Analysis 133 (1995) 129–144 (1995).

[24] G. Grün, On convergent schemes for diffuse interface models for two-phase flow of incompressible fluids with general mass densities, SIAM Journal on Numerical Analysis 51 (6) (2013) 3036–3061 (2013).

[25] H. Abels, D. Depner, H. Garcke, Existence of weak solutions for a diffuse interface model for two-phase flows of incompressible fluids with different densities, Journal of Mathematical Fluid Mechanics 15 (3) (2013) 453–480 (September 2013). doi:10.1007/s00021-012-0118-x.

[26] H. Abels, D. Depner, H. Garcke, On an incompressible Navier–Stokes / Cahn–Hilliard system with degenerate mobility, Annales de l'Institut Henri Poincaré (C) Non Linear Analysis 30 (6) (2013) 1175–1190 (2013).

[27] C. G. Gal, M. Grasselli, A. Miranville, Cahn–hilliard–navier–stokes systems with moving contact lines, Calculus of Variations and Partial Differential Equations 55 (3) (2016) 50 (May 2016). doi:10.1007/s00526-016-0992-9.

[28] P. Colli, G. Gilardi, J. Sprekels, On a Cahn–Hilliard system with convection and dynamic boundary conditions, Annali di Matematica Pura ed Applicata (2017) 1–31 (2017).

[29] X. Xu, Y. Di, H. Yu, Sharp-interface limits of a phase-field model with a generalized Navier slip boundary condition for moving contact lines, Journal of Fluid Mechanics 849 (2018) 805–833 (2018). doi:10.1017/jfm.2018.428.

[30] F. Guillén-González, G. Tierra, On linear schemes for a Cahn–Hilliard diffuse interface model, Journal of Computational Physics 234 (2013) 140–171 (2013). doi:10.1016/j.jcp.2012.09.020.

[31] J. F. Blowey, C. M. Elliott, The Cahn–Hilliard gradient theory for phase separation with non-smooth free energy. Part I: Mathematical analysis, European Journal of Applied Mathematics 2 (1991) 233–280 (1991).

[32] S. Hysing, S. Turek, D. Kuzmin, N. Parolini, E. Burman, S. Ganesan, L. Tobiska, Quantitative benchmark computations of two-dimensional bubble dynamics, International Journal for Numerical Methods in Fluids 60 (11) (2009) 1259–1288 (2009). doi:10.1002/fld.1934.

[33] X. Wu, G. van Zwieten, K. van der Zee, Stabilized second-order convex splitting schemes for Cahn–Hilliard models with application to diffuse-interface tumor-growth models , International Journal for Numerical Methods in Biomedical Engineering 30 (2014) 180–203 (2014). doi:10.1002/cnm.2597.

[34] H. Ding, P. Spelt, Wetting condition in diffuse interface simulations of contact line motion, Physical Review E 75 (2007) 046708 (2007).

[35] R. Backofen, S. Wise, M. Salvalaglio, A. Voigt, Convexity splitting in a phase field model for surface diffusion, International Journal of Numerical Analysis and Modeling (2018).

[36] M. Besier, W. Wollner, On the pressure approximation in nonstationary incompressible flow simulations on dynamically varying spatial meshes, International Journal for Numerical Methods in Fluids (2011). doi:10.1002/fld.2625.

[37] S. Minjeaud, An unconditionally stable uncoupled scheme for a triphasic Cahn–Hilliard/Navier–Stokes model, Numerical Methods for Partial Differential Equations 29 (2) (2013) 584–618 (March 2013). doi:10.1002/num.21721.

[38] D. Kay, V. Styles, R. Welford, Finite element approximation of a Cahn–Hilliard–Navier–Stokes system, Interfaces and Free Boundaries 10 (1) (2008) 15–43 (2008).

[39] F. Guillén-González, G. Tierra, Second order schemes and time-step adaptivity for Allen–Cahn and Cahn–Hilliard models, Computers and Mathematics with Applications 68 (8) (2014) 821–846 (2014).

[40] A. E. Diegel, C. Wang, S. M. Wiese, Stability and convergence of a second-order mixed finite element method for the Cahn–Hilliard equation, IMA Journal of Numerical Analyis 36 (2016) 1867–1897 (2016). doi:10.1093/imanum/drv065.

[41] L. Wang, H. Yu, On Efficient Second Order Stabilized Semi-implicit Schemes for the Cahn–Hilliard Phase-Field Equation, Journal of Scientific Computing 77 (2018) 1185–1209 (2018). doi:10.1007/s10915-018-0746-2.

[42] X. Yang, L. Ju, Linear and unconditionally energy stable schemes for the binary fluid-surfactant phase field model, Computational Methods in Applied Mechanics and Engineering 318 (2017) 1005–1029 (2017).

[43] X. Yang, H. Yu, Efficient second order unconditionally stable schemes for a phase field moving contact line model using an invariant energy quadratization approach, SIAM Journal on Scientific Computing 40 (3) (2018) B889–B914 (2018).

[44] M. Alnæs, J. Blechta, J. Hake, A. Johansson, B. Kehlet, A. Logg, C. Richardson, J. Ring, M. Rognes, G. Wells, The fenics project version 1.5, Archive of Numerical Software 3 (100) (2015). doi:10.11588/ans.2015.100.20553.

[45] A. Logg, K.-A. Mardal, G. Wells (Eds.), Automated Solution of Differential Equations by the Finite Element Method - The FEniCS Book, Vol. 84 of Lecture Notes in Computational Science and Engineering, Springer, 2012 (2012). doi:10.1007/978-3-642-23099-8.

[46] S. Balay, S. Abhyankar, M. F. Adams, J. Brown, P. Brune, K. Buschelman, L. Dalcin, V. Eijkhout, W. D. Gropp, D. Kaushik, M. G. Knepley, D. A. May, L. C. McInnes, R. T. Mills, T. Munson, K. Rupp, P. Sanan, B. F. Smith, S. Zampini, H. Zhang, H. Zhang. PETSc Web page [online] (2018).

[47] S. Balay, S. Abhyankar, M. F. Adams, J. Brown, P. Brune, K. Buschelman, L. Dalcin, V. Eijkhout, W. D. Gropp, D. Kaushik, M. G. Knepley, D. A. May, L. C. McInnes, R. T. Mills, T. Munson, K. Rupp, P. Sanan, B. F. Smith, S. Zampini, H. Zhang, H. Zhang, PETSc users manual, Tech. Rep. ANL-95/11 - Revision 3.9, Argonne National Laboratory (2018).

[48] S. Balay, W. D. Gropp, L. C. McInnes, B. F. Smith, Efficient management of parallelism in object oriented numerical software libraries, in: E. Arge, A. M. Bruaset, H. P. Langtangen (Eds.), Modern Software Tools in Scientific Computing, Birkhäuser Press, 1997, pp. 163–202 (1997).

[49] P. R. Amestoy, I. S. Duff, J. Koster, J.-Y. L'Excellent, A fully asynchronous multifrontal solver using distributed dynamic scheduling, SIAM Journal on Matrix Analysis and Applications 23 (1) (2001) 15–41 (2001).

[50] P. R. Amestoy, A. Guermouche, J.-Y. L'Excellent, S. Pralet, Hybrid scheduling for the parallel solution of linear systems, Parallel Computing 32 (2) (2006) 136–156 (2006).

[51] S. Aland, A. Voigt, Benchmark computations of diffuse interface models for two-dimensional bubble dynamics, International Journal for Numerical Methods in Fluids 69 (2012) 747–761 (2012). doi:10.1002/fld.2611.

[52] V. V. Khatavkar, P. D. Anderson, H. E. Meijer, On scaling of diffuse-interface models, Chem. Eng. Sci. 61 (8) (2006) 2364–2378 (2006). doi:10.1016/j.ces.2005.10.035.

[53] A. A. Donaldson, D. M. Kirpalani, A. Macchi, Diffuse interface tracking of immiscible fluids: Improving phase continuity through free energy density selection, Int. J. Multiph. Flow 37 (7) (2011) 777–787 (2011). doi:10.1016/j.ijmultiphaseflow.2011.02.002.

[54] C. Kahle, An L^∞ bound for the Cahn–Hilliard equation with relaxed non-smooth free energy density, International Journal of Numerical Analysis and Modeling 14 (2) (2017) 243–254 (2017).

[55] J. Bosch, C. Kahle, M. Stoll, Preconditioning of a coupled cahn–hilliard navier–stokes system, Communications in Computational Physics 23 (2) (2018) 603–628 (2018). doi:10.4208/cicp.OA-2017-0037.

[56] K.-Y. Law, Definitions for Hydrophilicity, Hydrophobicity, and Superhydrophobicity: Getting the Basics Right, J. Phys. Chem. Lett. 5 (4) (2014) 686–688 (2014). doi:10.1021/jz402762h.

[57] D. N. Sibley, A. Nold, N. Savva, S. Kalliadasis, On the moving contact line singularity: Asymptotics of a diffuse-interface model, Eur. Phys. J. E 36 (3) (2013). arXiv:arXiv:1210.1724v2, doi:10.1140/epje/i2013-13026-y.

[58] T. Omori, T. Kajishima, Apparent and microscopic dynamic contact angles in confined flows, Phys. Fluids 29 (11) (2017). doi:10.1063/1.4992014.